

EES Solar

Accepted Manuscript

This article can be cited before page numbers have been issued, to do this please use: F. Baumann, J. Padilla-Pantoja, J. M. Caicedo, M. Karimipour, N. Vahedigharehchopogh, J. Santiso, B. Ballesteros, R. Miranda, Z. Tian, S. R. Raga and M. Lira-Cantu, *EES Sol.*, 2025, DOI: 10.1039/D5EL00104H.



This is an Accepted Manuscript, which has been through the Royal Society of Chemistry peer review process and has been accepted for publication.

Accepted Manuscripts are published online shortly after acceptance, before technical editing, formatting and proof reading. Using this free service, authors can make their results available to the community, in citable form, before we publish the edited article. We will replace this Accepted Manuscript with the edited and formatted Advance Article as soon as it is available.

You can find more information about Accepted Manuscripts in the [Information for Authors](#).

Please note that technical editing may introduce minor changes to the text and/or graphics, which may alter content. The journal's standard [Terms & Conditions](#) and the [Ethical guidelines](#) still apply. In no event shall the Royal Society of Chemistry be held responsible for any errors or omissions in this Accepted Manuscript or any consequences arising from the use of any information it contains.

BROADER CONTEXT

View Article Online
DOI: 10.1039/D5EL00104H

Amid today's urgent push for sustainable energy, halide perovskite solar cells (PSC) have emerged as a promising renewable technology. Despite significant progress, PSC devices still struggle to exceed a one-year lifespan, falling short of industrial standards and limiting commercialization. Rapid detection of early degradation through accelerated testing over just a few hours can save time and resources, advancing PSC development more efficiently. The variety of dynamic processes and complex degradation pathways in PSC under operation conditions can only be understood through in-situ characterization. This study investigates the evolution of HP crystal lattice under applied bias, illumination and high temperature with a customized in-situ XRD setup. We show that targeted design modifications in the PSC can prevent light- and heat-induced perovskite amorphisation into a phase that creates new shunt paths and increases carrier losses. This work highlights the need for strategies that reinforces the crystal structure by targeting grain boundaries and mitigates thermal expansion mismatches through interfacial engineering.



ARTICLE

View Article Online
DOI: 10.1039/D5EL00104H

Stabilizing Perovskite Solar Cells at 85 °C via Additive Engineering and MXene Interlayers

Fanny Baumann,^a Jessica Padilla-Pantoja,^a Jose Manuel Caicedo-Roque,^a Masoud Karimipour,^a Naji Vahedigharehchopogh,^a Jose Santiso,^a Belén Ballesteros,^a Ramsés A. Miranda Gamboa,^a Zhenchuan Tian,^a Sonia R. Raga,^{*a} Monica Lira-Cantú^{*a}

Received 00th January 20xx,
Accepted 00th January 20xx

DOI: 10.1039/x0xx00000x

The commercialization of Perovskite Solar Cells (PSCs) is currently a reality. Now, the detection of early instabilities is vital for the successful widespread implementation of the technology. High temperatures and heating due to illumination, are highly relevant stress conditions for PSCs. Commercial devices must sustain temperatures as high as 85 °C in order to surpass standardization tests and certification for the final PV product. However, stability analysis and detailed structural and electronic properties of full devices is required, especially under in-situ and non-invasive conditions which are still rarely found in the literature. In this work, we carried out in-situ operational stability testing, complemented by in-situ X-ray diffraction, impedance spectroscopy, photoluminescence, current-voltage measurements and electron microscopy. Through parallel non-invasive characterization of full devices' structural and electronic properties and rigorous operational testing at 85 °C, the mechanisms driving performance degradation were revealed. A large thermal lattice expansion at 85 °C due to conduction and light induced heating leads to interfacial lattice strain which resulted in a voltage drop in the PSC. While no changes in lattice constants over time at constant conditions were observed, a reversible formation of a surface shell layer surrounding the perovskite grains is formed at 85 °C, and is linked to a decrease in shunt resistance, and the increase of ionic conductivity. The latter triggered the gradual photovoltaic performance loss observed in our PSC at high temperature. Additionally, we demonstrate the possibility to delay this PSC degradation by employing stability-enhancing methods such as additive engineering and the application of functionalized 2D Ti₃C₂ MXene interlayers to the PSC. Our work showcases the value of complementing stability tests with advanced characterization, significantly showcasing the value of in-operando structural studies.

Introduction

Before perovskite solar cells (PSC) can satisfy industrial needs with warranty for acceptable performance,^{2, 3} it is fundamental to mitigate photovoltaic loss under high temperature and variable light-irradiance conditions experienced under real operation.^{4, 5} Photovoltaic modules heat up to an average of ~45–50 °C and up to ~65 °C under operation.^{6, 7} At extreme conditions, such as space stations or satellites, both radiation and temperature levels are more intense, with temperatures up to 85 °C measured.⁸ 65 °C and 85 °C are the temperature thresholds defined in the ISOS consensus protocols for PSCs stability,⁹ and the IEC 61215 standard.^{10, 11}

Usually, high temperatures are reached at high irradiation, yet empirical calculations suggest that the internal heating of the perovskite layer might be higher than the measured module temperature.¹¹ Operational testing at illumination and elevated temperature might be more predictive of outdoor stability.^{12, 13} Both light and temperature provide excess energy into the PSC

system, which can destabilize the halide perovskite (HP) structure leading to material and device degradation. The extra energy in the PSC system may produce damaging structural effects in the HP,¹⁴ decrease ionic migration activation energies, and induce sequential degradation processes from intrinsic changes of the HP.^{15, 16} However, most studies on temperature-induced degradation only report local material changes in isolated single crystals or films, eluding the interactions of the selective layers, applied bias or photogeneration in the degradation, while the effects on device performance have been observed in separate experiments with post-mortem investigations eluding reversible phenomena. Here, we join local and general effects, to understand the initial degradation pathways of full PSC devices. In addition, the interplay between varying light intensity and temperature is not frequently reported for full devices but it is critical to get an accurate picture of mechanisms triggering degradation, particularly relevant for outdoor applications.^{17–19}

Successful strategies to mitigate PSC degradation at higher temperatures and illumination include compositional tuning, interlayers to avoid delamination, interfacial engineering, and molecular additives in the bulk.^{5, 20–23} Additives in the HP solution can induce changes in the film crystal orientation and relaxation of internal strain in the crystal grains.^{1, 21–23} Moreover, additives that incorporate in the bulk HP can lead to formation of 2D/3D structures. Recently, the use of additives that reside

^a Catalan Institute of Nanoscience and Nanotechnology (ICN2), CSIC and the Barcelona Institute of Science and Technology (BIST), Building ICN2, Campus UAB, E-08193 Bellaterra, Barcelona, Spain.

* Corresponding author emails: sonia.ruizraga@icn2.cat, monica.lira@icn2.cat
Supplementary Information available: [details of any supplementary information available should be included here]. See DOI: 10.1039/x0xx00000x



only at grain boundaries and surfaces is becoming more frequent.^{22, 24, 25} The phosphonate additive 3-phosphonopropionic acid (H3PP) had proven to passivate shallow defects and provoke a small compression in the perovskite lattice, with the consequence of improved stability at high illumination.^{1, 22} Similarly, interlayers including MXene-functionalized with the H3PP additive had proven to greatly improve stability of PSCs under outdoor testing.²⁶ However, the effect of these additions had not been analyzed at higher temperatures.

In this work, we investigated full PSCs devices under constant light irradiation of $\sim 100 \text{ mW/cm}^2$ (1 sun), in N_2 and at 85°C by operational tracking of maximum power point (MPPT) and with in-situ X-ray diffraction (XRD) while under bias near MPP. We compared state-of-the-art triple cation-based PSCs (REF) to modified devices (MOD) with additive engineering in the HP precursor and functionalized-MXene interfacial layer between the HP and spiro-OMeTAD. The HP and the MXene were both modified by adding the organic molecule 3-phosphonopropionic acid (H3PP).

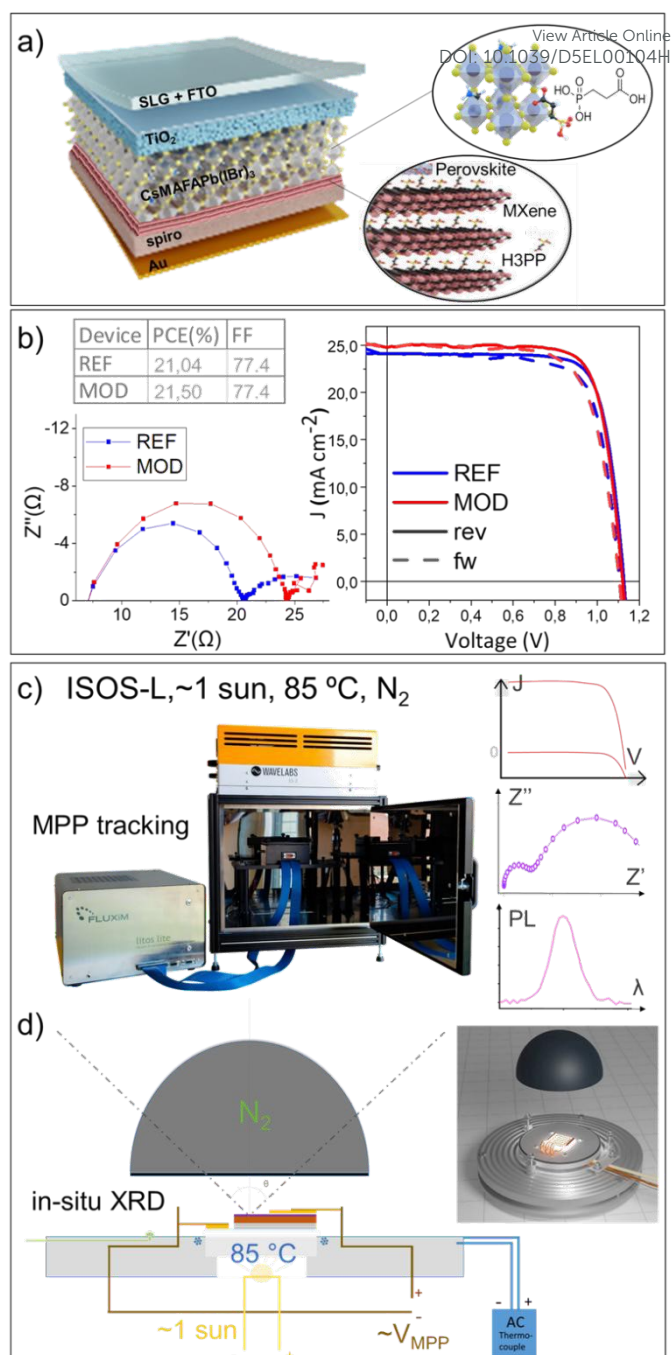
MPP Operational stability testing was complemented with characterization including in-situ X-ray diffraction (XRD) analyses of full devices during operational conditions, electrochemical impedance spectroscopy (EIS) at varying light intensities, photoluminescence (PL), current density – voltage (J - V), and transmission electron microscopy (TEM). This combination of advanced methods allowed us to identify simultaneous changes in lattice constants and electrical output at high temperature and illumination while correlating structural and performance changes with the observed electrochemical properties of the devices. We show how reversible stages of degradation in full devices at high temperatures induce structural transformations that facilitate inter-grain amorphization without formation of PbI_2 or lattice parameter evolution over time. This contrasts with previous works where PbI_2 is reportedly the end product of irreversible thermal degradation of perovskite crystals. Our results also show a photocarrier loss mechanism causing the MPP decay that is attributed to electrical shunt paths through the amorphous material originated at grain boundaries.

This work is, to our knowledge, the first study where structural dynamics by XRD and device performance is monitored jointly in full PSC devices under thermal conditions of 85°C and illumination stress.

Results and Discussion

Operational stability at 85°C with detailed characterization before and after (B&A)

Devices investigated in this work were produced with a standard recipe and with stability enhancing modifications for comparison. We produced control n-i-p solar cells with precursor composition $\text{Cs}_{0.08}\text{MA}_{0.12}\text{FA}_{0.8}\text{Pb}(\text{I}_{0.88}\text{Br}_{0.12})_3$ (FA:formamidinium, MA:methylammonium) and device stack $\text{FTO}/\text{TiO}_2\text{-c}/\text{TiO}_2\text{-mp}/\text{HP}/\text{spiro-OMeTAD}/\text{Au}$ (hereafter REF). Modified devices (hereafter MOD) incorporate the H3PP additive in the perovskite precursor and an interlayer of delaminated 2D MXene Ti_3C_2 functionalized with H3PP between the perovskite and the



HTM, having a final architecture: $\text{FTO}/\text{TiO}_2\text{-c}/\text{TiO}_2\text{-mp}/\text{H3PP:HP}/\text{H3PP:MXene}/\text{spiroOMeTAD}/\text{Au}$ (Figure 1a), with the corresponding champion photovoltaic performance shown in Figure 1b. Operational testing under 100 mWcm^{-2} spectral-matching LED illumination and at 85°C under maximum power point (MPP) operational stability test (ISOS-L2) with N_2 flow was endured for more than 20 h. Figure 1c shows the set up employed for stability analysis, and Figure 1d the home-made setup employed for in-situ characterization.



The power conversion efficiency (PCE) evolution at 85 °C under illumination in Figure 2b and the efficiencies before and after operational testing (Figure 2a and c, respectively) show that the modification with H3PP and MXene interlayer successfully improved stability in MOD PSCs, in accordance with previous observations at lower temperatures.^{22, 26} At these severer conditions, all PSCs of both varieties lose a significant part of their initial function, with MOD PSCs showing a more stabilized performance once at high temperature.

Figure 2d-e shows the corresponding J-V curves before and after MPPT testing, together with the V_{MPP} - J_{MPP} evolution (displayed as gradient-colored dots depending on time), hereafter MPP wandering plot. The MPP wandering plot lets us observe a different slope in the V_{MPP} - J_{MPP} changes over time; once the REF sample was operated at higher temperature the MPP voltage dropped progressively from 0.8 V to 0.7 V, before suddenly falling further to 0.6 V in the after J-V-scan (Figure 2d), while MOD

devices showed a 0.05 V initial improvement in V_{MPP} during the first hours of operation, followed by small accompanied voltage and current losses. V_{MPP} in REF decayed 0.1 V more (from 0.8 V to 0.6 V) compared to in MOD, where V_{MPP} even improved 0.05 V at the start of operation, followed by small voltage and current losses. We suggest this strategic way of presenting the MPP decay as it contains more information than only the PCE ($V_{MPP} \cdot J_{MPP} / P_{in}$).

Ionic and electronic changes. In order to reveal how the electronic and ionic mechanisms in our devices differed with the added modifications, we carried out electrochemical impedance spectroscopy (EIS), photoluminescence (PL) emission and time-resolved PL decay (TRPL) on all PSCs before and after the operational stress tests. EIS was measured at the open circuit voltage (V_{oc}) under a logarithmic array of light intensities from 0.001 to 103.5 mW/cm². Figure 3a displays the EIS data fitted to

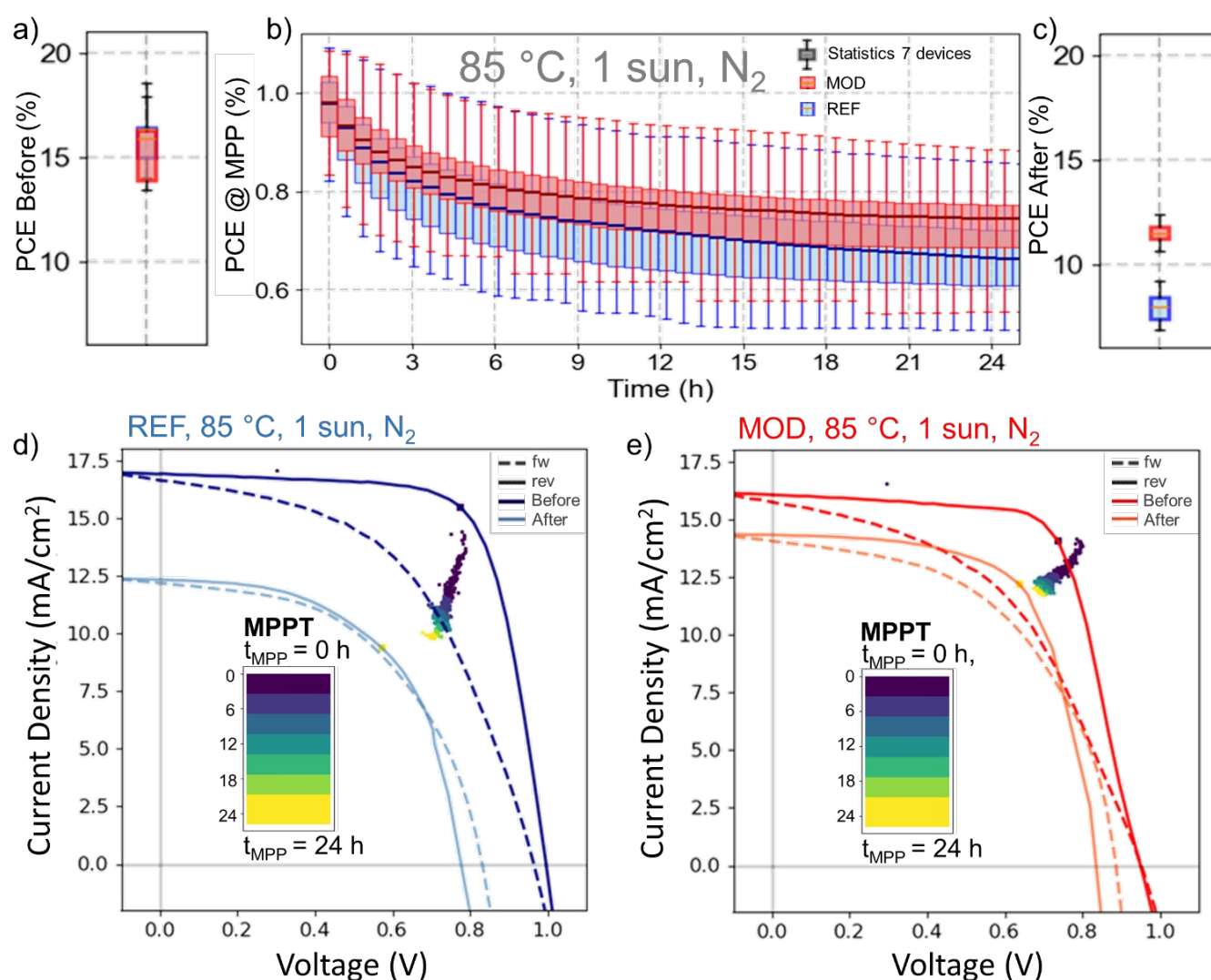


Figure 2. Operational stability test of PSCs analyzed at 85 °C and 100 mWcm⁻² (~1 sun) LED illumination using LITOS™ for seven REF PSCs (Blue) and seven MOD PSCs (red). (a) Power conversion efficiency (PCE) before operational testing for REF and MOD devices extracted from the J-V reverse scan measured under AM1.5G solar simulator. (b) LITOS™ MPP tracking at 85 °C, normalized to initiation of the test (boxplots marking the statistics include 7 PSC). (c) Power conversion efficiency (PCE) after operational testing for the same devices as in (a). (d)-(e) MPP wandering plot showing the change in V_{MPP} and J_{MPP} for two PSC of initial equal performance (in measurement shown in (a)), plotted on the before and after J-V curve taken immediately before (cold cells) and after (warm cells) MPP test, (d) without modification (REF) and (e) with MXene:H3PP interface and HP:H3PP bulk modification (MOD).



a standard Matryoshka circuit, as introduced by Bisquert *et al.*, (see Figure S1).^{27, 28} In high efficiency PSCs, the resistances extracted from the high- and the low-frequency (LF) Nyquist arcs (R_{HF} and R_{LF} , respectively) are attributed to a unique physical process in the perovskite, where the LF contribution originates from the phase-delayed electrical response by perovskite mobile ions. While parameters obtained from six different cells of each variation were very similar in all fresh devices (represented as grey symbols in Figure 3), a parameter distribution was found depending on device-to-device variation and the time that EIS was measured after the MPP test. The fitted EIS values PSC measured 10 min and 90 min after stress from each variation (MOD, REF) are represented by red circles and blue squares respectively, with cells measured in-between laying within the shaded red and blue areas (longer times shown in Figure S2).

EIS analyses show three main changes in MOD and REF devices measured after the high temperature operational test, compared to before.

The smallest (parallel) resistance has a predominant contribution to the resulting resistance value from EIS. Recombination resistance (R_{rec}) shows at high light intensities, while shunt resistance dominates in dark and low illumination. In Figure 3b, the resistances are represented as $R_{SUM} = R_{HF} + R_{LF}$.²⁹ First, a change in the recombination mechanisms in the perovskite film is deduced by reduced slope of R_{SUM} vs. V_{OC} (Equation S2) at the highest light intensities. The increased apparent-ideality-factor (n_{ap}) and the reduced intercept (R_0) observed, suggest higher recombination rates due to increased number of defect trap states after stress, resulting in lowered V_{OC} at high light intensities.³⁰ Second, at lower light intensities, a large decrease in R_{SUM} occurred in parallel to a V_{OC} drop at the low light intensity range. We recently identified this change as a shunt-like mechanism causing carrier loss within the perovskite film, named as perovskite shunt resistance (R_{psh}).²⁹ In contrast with traditional shunt resistance of a photovoltaic device, R_{psh} does not appear to have a constant value as would be found for an ohmic contact between the selective layers. Instead, R_{psh} depends on the electric field without simple exponential behavior, suggesting it is a material property of the perovskite film. The decrease in R_{psh} is significantly more severe for the REF devices, extending towards higher light intensities and competing with the R_{rec} signal even at the highest illumination. Third, a reduction of between one and three orders of magnitude of the low frequency time constant (τ_{LF}) (Figure 3c), $\tau_{LF} = C_{LF} \cdot R_{LF}$ (Equation S1), indicates increased ion conductivity, in-turn dependent on the ionic density and mobility.^{31, 32 33, 34, 35} After operation at 85 °C, both the REF and the MOD low frequency phase signal contribution (Figure S3) shifted right towards higher frequencies, leading to lower time constants (τ_{LF}) in the fittings (Figure 3c). This increase in ion-related contributions was retarded in MOD devices, particularly at lower light intensities.

Ion mobility or density simulations. When comparing the experimental EIS data through Nyquist and Bode-plots (Figure S3) with simple drift diffusion simulated data (Figure S4),^{18, 32} we found that the plot shifts observed could be better replicated

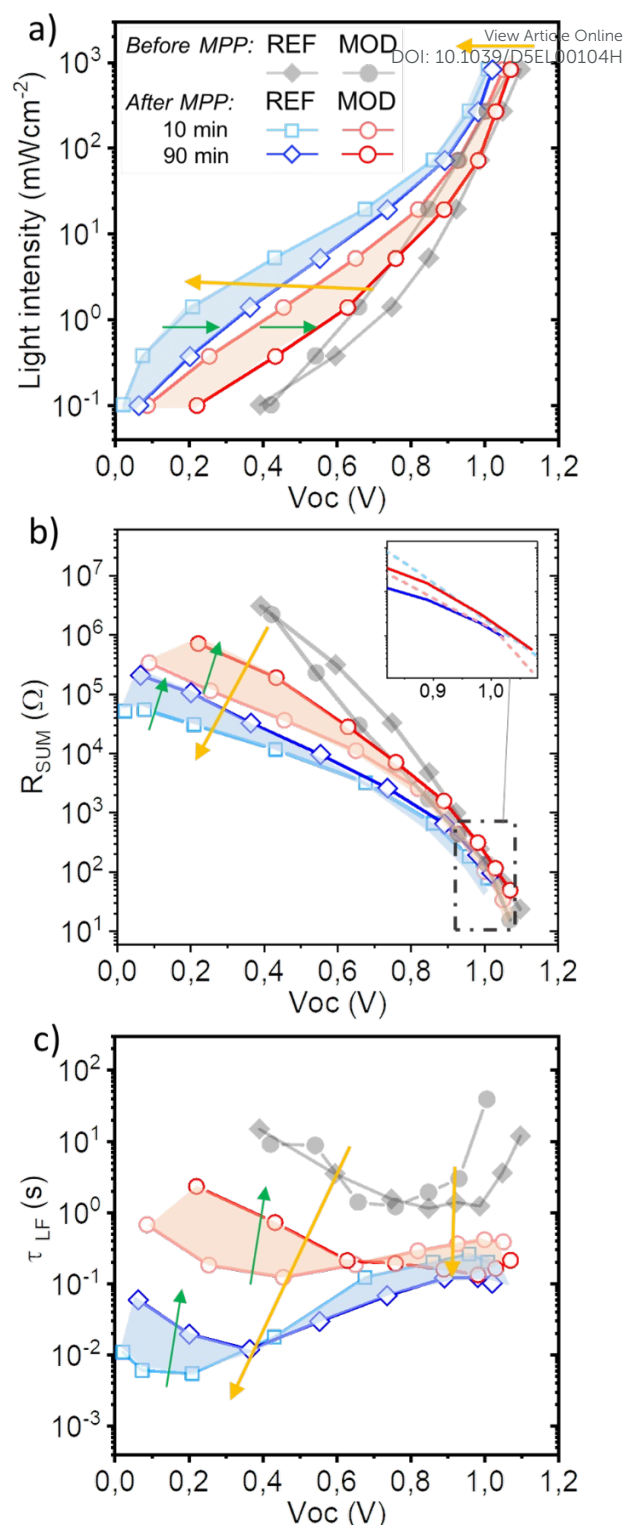


Figure 3. EIS at a logarithmic array of light intensities, before and after MPP operation at 85 °C for ~24 h. Values obtained from samples measured 10 min and 90 min after operation from each variation (MOD/REF) with shadowed approximate range of additional operated solar cells for visual guide. Yellow arrows mark the degradation trend. (a) Light Intensity/ V_{OC} relationship. (b) Total resistance $R_{SUM} = R_{HF} + R_{LF}$. (c) The low frequency time-constant, τ_{LF} . Dark green arrows mark the recovery phenomena of τ_{LF} depending on the time of EIS measurement after stress.



by increasing the cation mobility, rather than increasing the cation density (Figure S4).

We propose that the τ_{LF} changes could be related to the creation of high mobility channels for ions. It is worth noting that fresh devices before operation showed substantially higher τ_{LF} for MOD compared to REF PSCs, τ_{LF} extraction for MOD devices was particularly uncertain since the LF arc extended beyond the longest modulation wavelength measured. This indicates an initial effect of the H3PP and MXene modifications, possibly by hindering ionic channel pathways or bonding to loosen mobile ionic states (such as iodine vacancies) at the surfaces.³⁶⁻⁴¹ The remarkably low τ_{LF} , observed in REF PSCs measured immediately after stress, were jointly observed with effects of shunting seen on dark $J-V$ curves (Figure S2). Depending on how long time has passed after the operational test when the EIS was measured, both REF and MOD parameters showed a strong return towards initial values (reversibility). Still, MOD values showed a smaller initial change after stress, especially in these “recovering” regions (Figure 3c and Figure S2). The R_{psh} , R_{rec} , ion mobility increase, and V_{OC} drop appear to be reversible phenomena with some irreversible component, and the employed modifications interceded with these reversible processes.

In summary, the functionalized MXene and the presence of the bulk additive mitigated recombination and shunt losses after the high temperature stress test, resulting in higher V_{OC} retention than REF devices at high and low light intensities, respectively. The modification in PSCs led to an initially increased low frequency time constant (τ_{LF}), related to a lowered ionic conductivity on fresh devices, and minimized the decrease of τ_{LF} after temperature stress, in comparison with REF PSCs. Below, we reveal that abovementioned performance losses through R_{rec} , R_{psh} and τ_{LF} in REF can be attributed to the formation of a decomposition-related material located at the perovskite grain boundaries, which appearance is reduced in the presence of H3PP and MXene (in MOD devices).

Small bandgap changes and loss of generation. To relate the observed V_{OC} changes to possible changes in the perovskite bandgap, photoluminescence emission spectra (PL) was measured from the incident light side of the n-i-p solar cells before and after stress. No new peaks or protruding shoulders could be observed on PL emission spectra for either of the samples after stress, confirming that the perovskite did not undergo significant halide segregation or phase separation into any photo-emissive material.⁴² However, a ~6 nm blue shift in PL (fitted by a Gaussian function), Figure 4a and b, and a 5-fold drop in emission intensity was observed after the stress test. The decrease in PL intensity was coherent for both MOD and REF PSCs, with the blue shift being slightly more pronounced in the REF samples. As will be shown in XRD studies below, the thermal lattice expansion is similar in both MOD and REF, and HP lattices are not in an expanded state at the end of tests once thermal stress is removed. The PL blue shift after stress cannot be attributed to thermal expansion. While deep defects or structural changes would cause larger shifts, smaller PL shifts have been reported to stem from interaction with electron states close to the va-

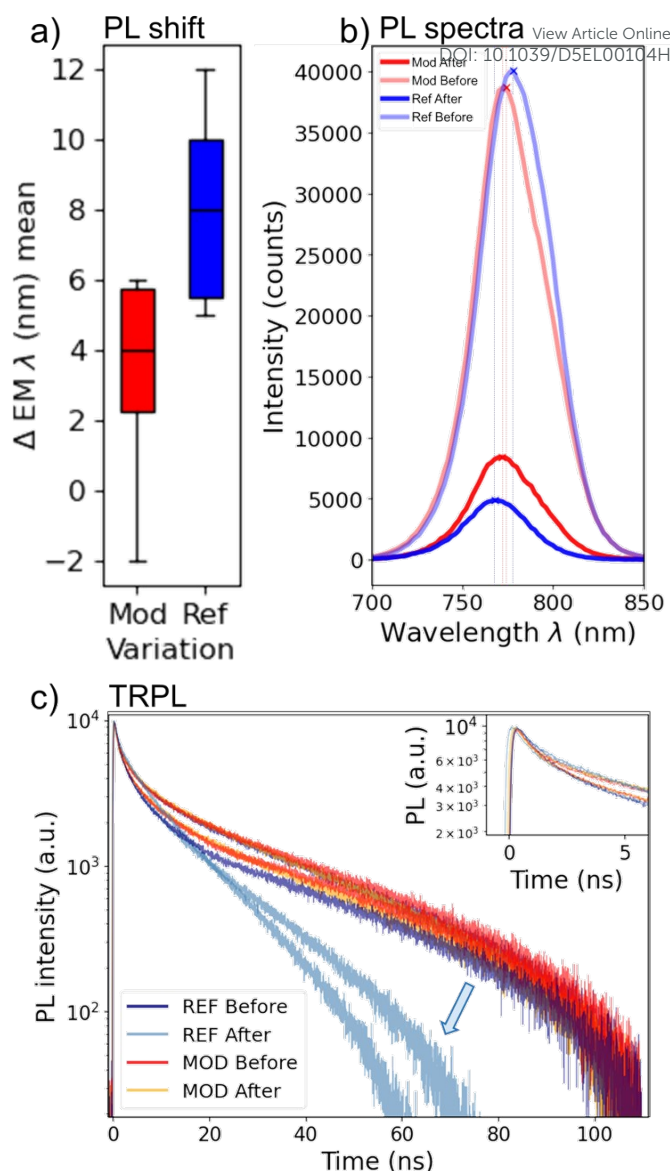


Figure 4. PL before and after operational testing at 85 °C.

(a) Statistical distribution of shift (Δ) in the Gaussian position fitting of PL spectra emission wavelength (EM λ). A mean of spectra positions acquired before and after TRPL, compared before and after operational stability. (b) an example of PL spectra to visualize the PL intensity drop after operation. (c) TRPL of two representative REF/MOD PSC taken before and after operational stability at 85 °C, showing how the REF PSCs lose luminescence intensity at longer timescales.

lence- and conduction- band, such as electron–phonon interactions, conversion of shallow defects to non-radiative interaction, and cation migration.⁴³⁻⁴⁵ Additional support that the blue shift is defect-related was seen by TRPL (Figure 4c). We assign the reduced signal at longer lifetimes to trap-mediated paths in the radiative recombination process, apparently higher in REF than in MOD after stress. This is probably due to a loss of photoactive material, defective photo-generating pathways or shallow defect reactions.⁴⁶

In-situ structural and performance evolution at 85 °C.



By employing a custom-made X-ray diffraction (XRD) holder (Figure 1b) in a common use XRD parallel beam setup under similar conditions and timeframe as the MPPT test, operational testing could be coupled with the structural evolution in full PSC devices. XRD scans were acquired continuously over a timeframe similar to the MPP study while monitoring the device electronic output by J - V curves and current output at approximate V_{MPP} . Structural effects were induced independently by the heating stage (low (27 °C) and high (85 °C)), and from illumination (dark and at 100 mWcm⁻²), all at constant N₂ flow enclosed by a graphite dome. Illumination was shone from the solar cell glass side by a white LED (Figure S1a) calibrated to produce a similar I_{SC} as at 1 sun AM1.5G conditions.

Figure 5 shows gathered structural and performance data for two PSC, one REF and one MOD PSC, through stages of the experiment including varied light and heat, and the main and longest stress block at 85 °C and 105 mW/cm² illumination for over 10 h. The experiment can be summarized in five stages as follows:

1. Dark at room temperature (RT, 27 °C) (Figure 5a-Stage 1)
2. Subsequent light and temperature addition from RT to 85 °C, and repeatedly turning the light on and off (Figure 5a-Stage 2)
3. Holding the temperature at 85 °C under illumination overnight for over 10 hours (Figure 5a-Stage 3)
4. Cool-down and light on and off (Figure 5a-Stage 4)
5. Switching the illumination on/off at RT and comparison of illumination and conductive heating (Figure 5a-Stage 5)

We observed that the integrity of all crystalline HP is maintained throughout the experiment with only different degree of isotropic thermal expansion independent on time, while the average intensity of all XRD peaks from the REF sample showed a small gradual decrease at 85 °C and illumination (Figure 5c), indicating that a small part of the perovskite crystal is gradually lost. On the contrary, the MOD sample, where grains are surrounded by the H3PP molecule and the MXene, did not show case this decrease (Figure 5c and S7b). This HP peak intensity decrease was the only crystalline change observed in the HP in agreement with the gradual performance (PCE) decrease observed for the REF sample (Figure 5d). Our results suggest that while part of the perovskite material is converted into a non-crystalline component, the crystalline integrity of the remaining HP is maintained.

Upon applying the illumination, a discrete 2θ left shift was seen in all perovskite diffraction peaks (Figure S5), indicating an increase of the lattice parameter (Figure 5b), while peaks from the substrate (fluoride doped tin oxide (FTO)), remained unaffected (Figure S7). When the set temperature was elevated to 85 °C, a second larger shift was noted, consistent with the known effect of thermal lattice expansion.⁴⁷ The lattice parameter at 85 °C and illumination remained steady along a ~14h period, without additional changes in PbI₂ content or the creation of new crystalline features (Figure S7a). After fitting all perovskite peaks with a Pseudo Voigt function and applying Nelson-Riley regression to obtain the lattice parameter (a) at the time of each measurement, no deviation from cubic structure was detected in any of the conditions, including no major changes in

microstructure (Figure S7c). Surprisingly, apart from an initially smaller lattice parameter in the MOD devices, the magnitude of the changes observed in the a -value for REF and MOD were the same, within the resolution of the experiment. Both REF and MOD HP lattice parameters transitioned between different seemingly discrete values (a jump up slightly below 0.01 Å from the illumination and ~0.02 Å when heating from 27 to 85 °C) (Figure 5a-b, Figure S6). Once stabilized at higher temperatures, the gradual loss in peak intensity seen on the XRD (at around 6-16 h in Figure 5c, stage 3) can be linked to the gradual decrease in the PCE output observed for REF (Figure 5d stage 3, to below 10%) under continued exposure to 85 °C heating and ~100 mWcm⁻² LED illumination. The PCE of the MOD device shows a flat curve upon prolonged exposure to the harsh conditions (Figure 5d), indicating that the performance of MOD devices is better maintained at higher temperature than for the REF devices, in agreement with the response observed under the stability analysis shown in Figure 2, under the ISOS-L3 protocol.

The J - V data measured during the in-situ XRD (Figure 5d-h) provided additional understanding of performance consequences of the crystalline changes, and accentuated the importance of the MXene:H3PP interlayer in MOD solar cells.⁴⁸ J - V curves taken before and after stress in XRD (Figure 5e-f, J - V curve A and E), correspond well to J - V curves observed before and after stability tests under MPP tracking, however, the changes observed on J - V curves for the REF sample *during* stress were much larger than expected. We observed an initial sharp drop in V_{OC} (Figure 5e, J - V curve B) when raising the temperature up to 85 °C, this response is also observed in the calculated power conversion efficiency of the REF sample (Figure 5d, J - V curve B). V_{OC} -loss is a common trend upon operation of PV at higher temperatures, but the detected drop of above 0.2 V (Figure 5e, J - V curve B) for REF solar cells is double that reported in previous works.⁶ During the lengthening of interatomic distances taking place upon thermal lattice expansion, as observed in Figure 5b, the tightly bound HP/HTM interface could lose contact or band-alignment, causing the voltage drop observed in Figure 5d-f.^{47, 49} Strain compensation by the mesoporous TiO₂ layer in the identical device structure has been observed as a lack of residual strain transfer from the FTO layer to the HP after glass cool down post-fabrication in our previous work.¹ It is possible that the MXene provides a similar function, leading to a lack of strain response in the MOD devices as both interfaces at the ETL and HTL sides of the perovskite may compensate the interfacial strain produced during heating. At the heat-up, during stage 2, the PCE of both REF and MOD samples showcased a drop of 50% and 25 %, respectively, a change in the initial efficiency from 20% to 10% for the REF sample and from 20% to 15% for the MOD sample. However, the fast drop is followed by a fast recovery of the efficiency in the REF sample, from 10% to 12% (Figure 5d-e J - V curve C). However, the sudden drop and fast recovery of the efficiency detected for the REF sample is not observed when the use of the MXene:H3PP interlayer is employed, an indication of the beneficial effect of the MXene interface which reduces this effect in half or completely prevents the sharp drop, possibly preventing future device degradation (Figure 5d,f J - V curves A, B, C).⁵⁰



Both REF and MOD solar cells transition to inverted hysteresis at 85 °C (Figure 5e-f, *J-V* curves B-D).⁵¹ In addition to MOD showing a smaller drop of V_{OC} upon raising the temperature, we also observe a smaller hysteresis. While the REF sample undergoes a large increase in the hysteresis index, not stemming from reduced fill factor, but rather from a 100-150 mV gradually lower V_{OC} in the reverse scan direction (at speed 40 mV/s, Figure 5e, *J-V* curves C-D), the absolute hysteresis index at 85 °C remains relatively small in the MOD device (Figure 5f, *J-V* curves C-D). Hysteresis is known to originate as a combination of factors related to electrode poling or ionic accumulation at the interface with the selective contact, modulating the internal electric field and altering the carrier transport and extraction.⁵²⁻⁵⁴ Despite that the exact mechanisms of hysteresis remain elusive, we attribute the increase in hysteresis in REF to the temperature - increased ionic motion inside the perovskite layer, in accordance with the lowered τ_{LF} seen in EIS. The increased mobility would result in larger ionic build-up, widening the depletion layer near the contacts. Thermal expansion (Figure 5b) is likely accompanied by a significantly wider perovskite band gap.^{48, 55} As a consequence, both interfacial band bending and wider gap will affect the band alignment between the perovskite and the

selective contacts, probably originating the *J-V* changes and inducing inverted hysteresis. The retained small hysteresis found in MOD is likely due to the hindered ion migration through the layer, also shown by larger τ_{LF} values from EIS, and prevention of the formation of an interfacial depletion layer by the MXene interlayer. Additionally, REF PSC dark *J-V* shows lower shunt resistance (Figure 5e) than MOD (Figure 5f), in line with our results from EIS. Upon cooling, the REF *J-V* reverse scan recovers to a point of similar V_{OC} as the forward scan, with similar inverted hysteresis as MOD but with both lower current and voltage output (Figure 5e-f, *J-V* curves D-E).

To summarize, in-situ XRD revealed two mechanisms of PSC loss at 85 °C; the first related to interfacial strain response during thermal expansion, the second to loss of crystalline HP.

At 85 °C, thermal lattice expansion leads to interfacial strain that produces a (partially reversible) voltage drop, and the use of MXene:H3PP interlayer greatly prevented this effect. However, the main cause of the gradual performance decay at 85 °C, was revealed to be the gradual loss of crystallinity in the bulk HP.

Upon cooling, partial peak recovery in REF (Figure 5c) suggests recrystallization, implying the degraded phase remains in

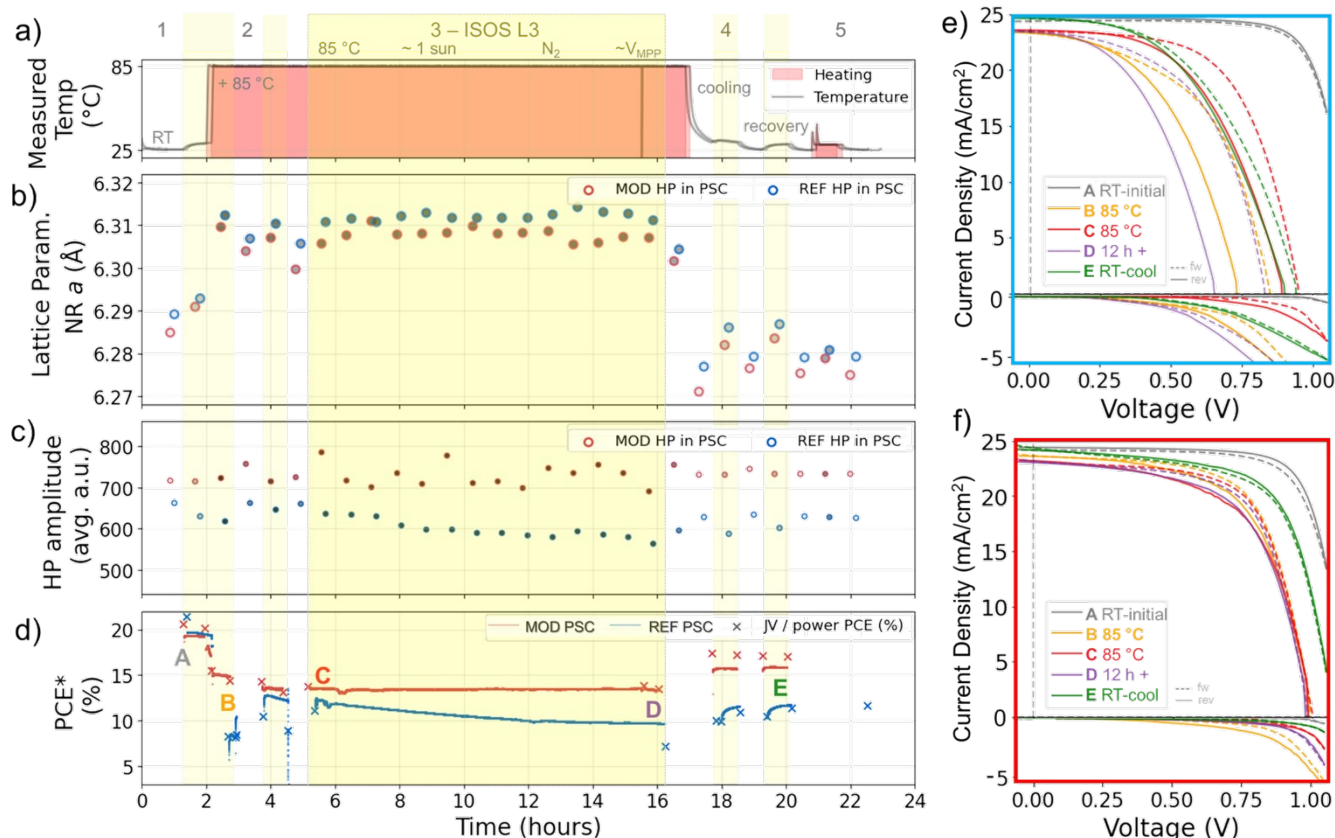


Figure 5. Simultaneous structural and operational changes during in-situ XRD of 2 devices, reference PSC (REF) and PSC with bulk HP:H3PP additive modification and MXene:H3PP interface modification (MOD). The output is shown only for the connected pixel, while the area of XRD is outside of the biased area (See Figure 1b). (a) Temperature setting and measured temperature, top marked 5 key stages during the experiment. (b) Lattice parameter from y-axis intercept in Nelson-Riley fitting (Figure S4) of XRD scans at 45 min intervals, (c) average amplitude of collective HP peaks on each XRD scan. (d) PCE calculated from output current density at approximated V_{MPP} and *J-V* curves, the yellow shade encompassing a) b), c) d) indicates the periods where light is on. (e-f) Selection of *J-V* curves (marked A-E in d) taken at 40 mV/s to show diode progression for the MOD device (red) and for REF device (blue), and *J-V* curves in dark conditions, closest to the points in the approximate PCE plot of *J-V*s (e) MOD (f) REF. fw- forward scan, rev- reverse scan.



the film, but is undetectable by our XRD measurements. The HP structural evolution directly impacts device PCE, which also shows partial reversibility. In the presence of the MXene and H3pp additive (MOD device), HP XRD peaks did not decline, and the earlier degradation of the PSC, observed in the REF device, was prevented.

Our results from EIS, PL and in-situ XRD are in agreement with separate observations of modified ionic movement, the appearance of inversed hysteresis, apparent shunting dependent on the electric field, and increased recombination and interface delamination above temperature thresholds.⁵⁶⁻⁶⁶ This is the first time these phenomena are reported jointly on the same timeline, revealing their direct connection.

Morphology investigations.

In order to reveal more about the morphological consequences of the crystal decomposition observed in the REF solar cells during XRD analysis, we employed ex-situ complimentary transmission electron microscopy (TEM) with energy dispersive X-ray spectroscopy (EDX), and cross section scanning electron microscopy (CS-SEM). Solar cells from the same batch as in Figure 5 were split in two in preparation for CS-SEM (Figure S8) and investigated with and without treatment at $\sim 100 \text{ mWcm}^{-2}$ and 85°C under high N_2 flow for 20 hours. After testing, HP samples were obtained by scratching the surface of the PSC, and the resulting powder was analyzed by HRTEM (Figure 6a-f).

HRTEM of un-treated MOD and REF HP samples (Figure S9) looked similar with clear distinguishable HP grains, as expected.

However, the REF sample treated at 85°C showed an outer “shell” layer enclosing the HP crystallite grains (Figure 6a-c and Figure S10). This core-shell nanostructure encompasses a well-crystalline HP grain in the inside (as confirmed by EDX, Figure S11), while the outside or the “shell” is characterized by a transparent and amorphous surface layer surrounding the HP grains, that would also be undetectable by XRD (colored in purple in Figure 6a-c, Figure S10). In addition, the treated MOD HP sample is observed to be more isolated with more easily resolved grains, despite a very scarce presence of another material (colored in green in Figure 6d-f, Figure S10). The maintained intensity of peaks observed in XRD for the MOD HP sample after treatment, together with the very occasional presence of the amorphous phase already observed in the REF sample, indicates that, in MOD, the employment of the organic molecule H3PP circumvents and delays the formation of the amorphous “shell” on the surface of the grains. This mitigation is probably due to the strong interaction between the H3PP molecule and the HP that could immobilize ions²², maintaining the integrity of the crystalline HP. Further investigation with EDX (Figure S11) showed that the “shell” material had a high carbon content. We deduce that the large A-site organic cation, being the only available source of carbon in the HP material, should be highly involved in the creation of the decomposition product. Even if formation of a new material or defects (Figure S12) was not completely prevented in MOD, the morphology and make-up of the two materials were vastly different. New phase regions in MOD had particles imbedded in the dimmer amorphous area as seen in TEM (Figure S10) and STEM (Figure S11). EDX of the bright

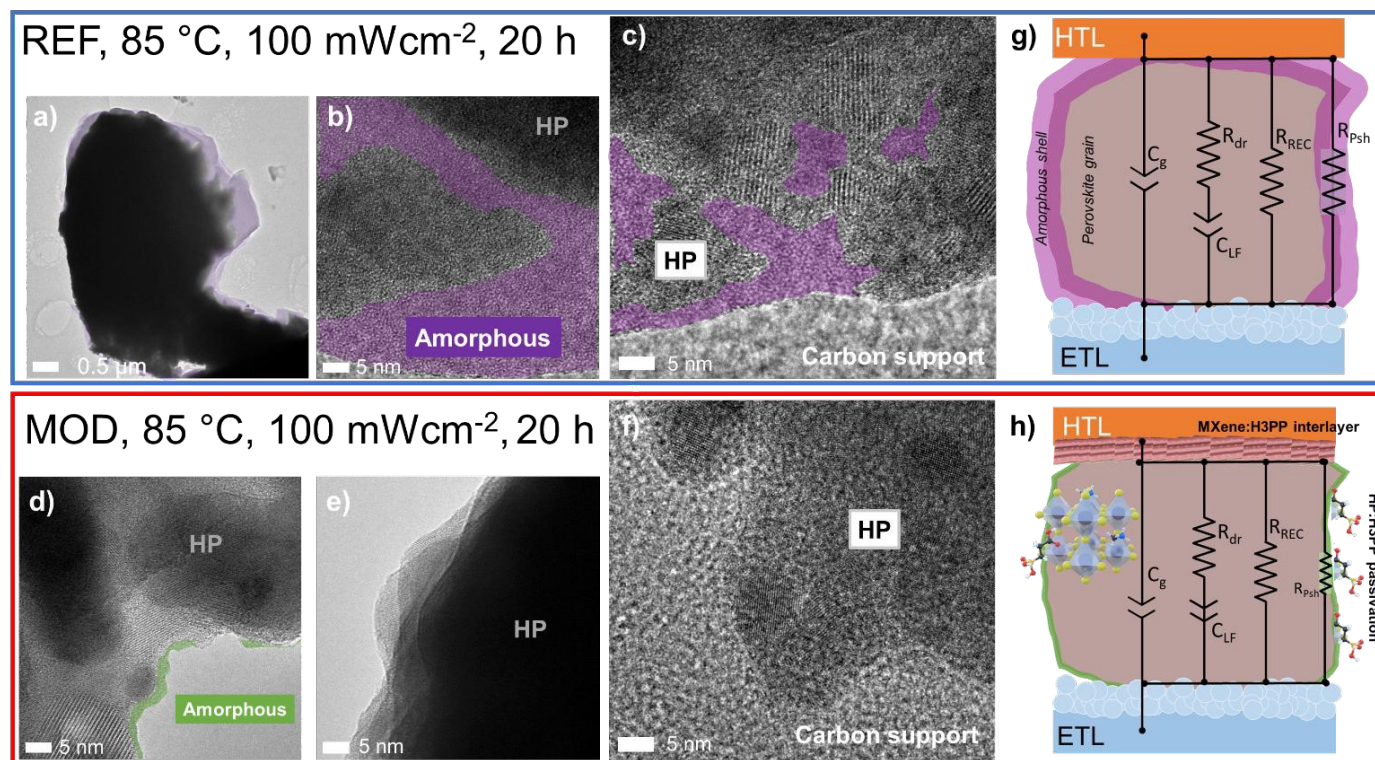


Figure 6. Selection of TEM images of HP from PSC treated at $\sim 105 \text{ mWcm}^{-2}$ and 85°C 1 week before TEM experiments. (a)-(c) HP from the treated REF solar cell half, with amorphous shell layer shaded purple. (d)-(f) HP from the treated MOD solar cell, with small shell shaded green. (g) REF PSC schematic showing how an amorphous material has been created around HP, leading to additional shunt paths, while in (h) MOD HP, most areas do not show the amorphous layer.



particles revealed that they contained strong Ti and O signals together with components of the HP, indicating a likely mixture of $\text{TiO}_2/\text{MXene}$ and HP. The MOD HP samples also showed a stronger titanium and oxygen signal, likely from the added content of titanium carbide from the MXene layer, indicating a close contact between the MXene layer and the perovskite.

Extended discussion.

As previously detailed, we observed that reversible processes in the HP material can be related to the PSC device's performance. Creation of amorphous-like regions in devices occurs before the irreversible step of PbI_2 formation. Our observations of an amorphous "shell" layer around HP are in accordance with previous studies made by TEM, that agree with the layer by layer decomposition from the surface of the perovskite grains at 85 °C previously reported.⁶⁷⁻⁷⁰ It has been reported that the presence of intermediate, amorphous like, areas of MAPbI_3 with what looks like ionic channels facilitate the reverse intercalation of MAI and PbI_2 , and that the appearance of PbI_2 is frequently related to ion migration, specifically of the large cation.^{71, 72,70, 73,74} In our experiments we do not observe any significant PbI_2 formation (Figure S7a), instead, we observe that the amorphous material formed during operation at 85 °C has a very high carbon content (Figure 6g), which implicates the involvement of the large organic cations. In addition, it is possible that this material can facilitate both fast electron and ion diffusion.^{75, 76} Faster electron and ion transport in this new amorphous phase is coherent with changes observed on the photovoltaic performance of the solar cells (Figure 2, Figure 5) and the EIS signal changes after stress (Figure 3) that indicate reversible formation of shunts; conductive channels (R_{psh}), and increased ion mobility (decreased τ_{LF}). The findings of the formation of this core-shell material observed after treatment at 85 °C, are in good agreement with the observed conductivity and mobility increases measured by the EIS analysis (Figure 3) and seen on in-situ *J-V* curves (Figure 5e),⁷⁷ which are smaller in the presence of H3PP and MXene (in MOD devices). This effect is represented by the electric circuits shown in Figure 6g-h that accentuate the shunt paths created by the amorphous phase.

We propose that the carbon-rich amorphous shell formed around the perovskite grains supposes highly conductive channels leading to both lower barriers for ionic migration (lower τ_{LF}) and electrical shunt-losses (lower R_{psh}). Ab initio calculations have shown that surface defects dominate the paths for ion migration in lead-iodide perovskites due to surface-assisted formation of migrating defects.⁷⁸ We show that the presence of these defects relates to the reversible formation of a surface layer in the HP, that leads to 3-fold increased ion conductivity, likely due to increased ion mobility. With the grain surface passivation by organic additive H3PP the migration in the shallow defects in the surface can be partially prevented resulting in enhanced stability. The ab-initio calculations support that the prevention of access to shallow trap states seen by passivation with H3PP,²² can be synonymous with the prevention of both ion migration and shallow trap state propagation. At higher temperatures, this new "shell material" surrounding the HP grains seems

to lead to further voltage drops and shunting-like features similar to what was seen on EIS and during operational testing. The recovery of XRD intensity upon removal of the heating explains the reversibility in efficiency as the shell converts back into crystalline perovskite. Therefore, the new "shell" formed around the HP grains is likely responsible for the reversible component seen by EIS. Incorporation of the H3PP molecule in the precursor of HP prevents its amorphization as the intensity of XRD at higher temperature is not gradually lost, yet it seems like if any material is formed its properties could be different, leading to a different loss-in-performance behavior.

Although the general voltage drop in MOD devices is concerning, it is a common trend upon operation of PV at higher temperatures.⁶ Even if additional voltage drops might still occur, we show how further improvements in grain boundary passivation and interfacial dynamics at varying temperature and illumination to account for changes could reduce the problems faced in these conditions. All factors considered, we could relate the morphological and crystalline changes occurring to electronic effects observed. Our study shows the value of simultaneous data-acquisition to arrive at certainty of the effects of observed changes both electronically and in physical and chemical properties.

Conclusions

In conclusion, we carried out stability analysis of PSCs at 85 °C and white LED light (~100 mWcm⁻²) illumination under operational testing with MPP tracking. Analyses were carried out under in-operando XRD testing conditions for n-i-p devices with and without additive engineering (passivation with H3PP additive) and functionalized with MXene interlayers between the perovskite and the HTM. Our findings reveal that perovskite lattice expansion occurs under conductive heating of the device and, additionally, from illumination-induced heat, independent of the surface temperature level. The expansion observed in the bulk of the perovskite was non-differentiable when molecular additives were employed. Instead, the difference in degradation seen during MPPT was due to a gradual transformation of the HP without additive into an amorphous phase around the crystal grains that appears as a carbon-rich layer. The formation of this "shell" was directly related to an increase in ionic conductivity, shallow trap state propagation and apparent shunting of devices, all partially reversible. Detailed EIS analysis revealed increased ionic conductivity and lowered shunt resistances, related to the creation of ionic and electronic conductive paths through the device, a phenomenon delayed by the phosphonate-group based additive at grain boundaries. The direct observation of the surface-induced decomposition and performance decay together when employing in-situ XRD, provides proof that paths are located at the surfaces of grains. In addition, we demonstrate that the functionalized-MXene interlayer protects the interface during thermal expansion to partially prevent voltage loss. The results provide a framework for future efforts with the aim of stabilizing perovskite solar cells under high temperature operation. Additionally, interfacial effects be-



tween the (expanding) perovskite and HTM layer created an additional sharp, temporary, voltage drop during changing temperature, and MXene interlayers can aid in compensating for problems caused by interfacial strain, with a result of higher solar cell stability.

Author contributions

F.B. performed the stability testing, additional measurements and experiments, and prepared the manuscript under supervision by S.R. and M.L.C. J.P.P. operated the XRD and J.P.P. and J.S. helped with XRD experimental design and analysis. S.R. created the EIS protocol, operated by F.B. F.B. designed data collection, collected data and wrote analysis code. J.M.C.R. fabricated the XRD stage with partial support from F.B. N.V. performed the CS-SEM acquisition, B.B. performed the TEM acquisition. M.K. fabricated the solar cell devices with assistance from Z.H. M.L. and S.R. secured the funding for the project and advised on the objectives. All authors contributed in discussions about results, and made comments on the manuscript.

Conflicts of interest

There are no conflicts to declare.

Data availability

The data supporting this article have been included as part of the ESI. Data for this article, including the raw data for all figures in the article are available at CORA - Research Data Repository (RDR) at [<https://doi.org/10.34810/data2409>].

Acknowledgements

The authors acknowledge the Spanish Ministry of Science and Innovation for the predoctoral contract to F.B. with Reference No. PRE2020-092669 of the Project No. SEV-2017-0706-20-3 and the contract of N.V. with ref. PRE2022-103001 of the project CEX2021-001214-S-20-6. This work constitutes part of the Materials Science Ph.D. Program for F.B., N.V. and Z.T. at the Universitat Autònoma de Barcelona (UAB, Spain). This project was funded by the project PerMXSol (ref. PID2022-143344OB-I00) and project grant TAMPOPO, (ref. PID2021-122349OAI00) funded by MCIN/AEI/10.13039/501100011033 and "ERDF A way of making Europe. ICN2 is funded by the CERCA Programme/Generalitat de Catalunya. Thanks to Agència de Gestió d'Ajuts Universitaris i de Recerca for Grant No. SGR 01617 and the Xarxa d' R + D + I Energy for Society.

The ICN2 is supported by the Severo Ochoa Centres of Excellence programme, Grant CEX2021-001214-S, funded by MCIN/AEI/10.13039/501100011033.

We would like to acknowledge the team from Syre (syre.ai), especially Dr. Brian Carlsen, for lending us their software prototype facilitating steps in the automatic processing of results from experiments. We would like to thank Damaso Torres for

his aid with graphic design, and Rafael León Lavín for modifications of the XRD holder and LITOS customized sample stages.

Notes and references

1. F. Baumann, M. Karimipour, J. Padilla-Pantoja, E. Chávez-Angel, J. M. Caicedo Roque, R. Pouteaux, A. Alcalá Ibarra, S. R. Raga, J. Santiso and M. Lira-Cantu, *ACS Energy Letters*, 2025, **10**, 476-483.
2. S.-P. Feng, Y. Cheng, H.-L. Yip, Y. Zhong, P. W. K. Fong, G. Li, A. Ng, C. Chen, L. A. Castriotta, F. Matteocci, L. Vesce, D. Saranin, A. D. Carlo, P. Wang, J. Wei Ho, Y. Hou, F. Lin, A. G. Aberle, Z. Song, Y. Yan, X. Chen, Y. Yang, A. A. Syed, I. Ahmad, T. Leung, Y. Wang, J. Lin, A. M. C. Ng, Y. Li, F. Ebadi, W. Tress, G. Richardson, C. Ge, H. Hu, M. Karimipour, F. Baumann, K. Tabah, C. Pereyra, S. R. Raga, H. Xie, M. Lira-Cantu, M. V. Khenkin, I. Visoly-Fisher, E. A. Katz, Y. Vaynzof, R. Vidal, G. Yu, H. Lin, S. Weng, S. Wang and A. B. Djurišić, *Journal of Physics: Materials*, 2023, **6**, 032501.
3. S. He, L. Qiu, L. K. Ono and Y. Qi, *Materials Science and Engineering: R: Reports*, 2020, **140**, 100545.
4. T. J. Jacobsson, A. Hultqvist, A. Garcia-Fernandez, A. Anand, A. Al-Ashouri, A. Hagfeldt, A. Crovetto, A. Abate, A. G. Ricciardulli, A. Vijayan, A. Kulkarni, A. Y. Anderson, B. P. Darwich, B. W. Yang, B. L. Coles, C. A. R. Perini, C. Rehermann, D. Ramirez, D. Fairen-Jimenez, D. Di Girolamo, D. L. Jia, E. Avila, E. J. Juarez-Perez, F. Baumann, F. Mathies, G. S. A. Gonzalez, G. Boschloo, G. Nasti, G. Paramasivam, G. Martinez-Denegri, H. Nasstrom, H. Michaels, H. Kobler, H. Wu, I. Benesperi, M. I. Dar, I. B. Pehlivan, I. E. Gould, J. N. Vagott, J. Dagar, J. Kettle, J. Yang, J. Z. Li, J. A. Smith, J. Pascual, J. J. Jeronimo-Rendon, J. F. Montoya, J. P. Correa-Baena, J. M. Qiu, J. X. Wang, K. Sveinbjornsson, K. Hirslandt, K. Dey, K. Frohna, L. Mathies, L. A. Castriotta, M. H. Aldamasy, M. Vasquez-Montoya, M. A. Ruiz-Preciado, M. A. Flatken, M. V. Khenkin, M. Grischek, M. Kedia, M. Saliba, M. Anaya, M. Veldhoen, N. Arora, O. Shargaieva, O. Maus, O. S. Game, O. Yudilevich, P. Fassl, Q. S. Zhou, R. Betancur, R. Munir, R. Patidar, S. D. Stranks, S. Alam, S. Kar, T. Unold, T. Abzieher, T. Edvinsson, T. W. David, U. W. Paetzold, W. Zia, W. F. Fu, W. W. Zuo, V. R. F. Schroder, W. Tress, X. L. Zhang, Y. H. Chiang, Z. Iqbal, Z. Q. Xie and E. Unger, *Nature Energy*, 2022, **7**, 107-115.
5. Y. Zhao, J. Zhang, Z. Xu, S. Sun, S. Langner, N. T. P. Hartono, T. Heumüller, Y. Hou, J. Elia, N. Li, G. J. Matt, X. Du, W. Meng, A. Osvet, K. Zhang, T. Stubhan, Y. Feng, J. Hauch, E. H. Sargent, T. Buonassisi and C. J. Brabec, *Nature Communications*, 2021, **12**, 2191.
6. M. Jošt, B. Lipovšek, B. Glazar, A. Al-Ashouri, K. Brecl, G. Matič, A. Magomedov, V. Getautis, M. Topič and S. Albrecht, *Advanced Energy Materials*, 2020, **10**, 2000454.
7. M. Koehl, M. Heck, S. Wiesmeier and J. Wirth, *Solar Energy Materials and Solar Cells*, 2011, **95**, 1638-1646.
8. G. A. Landis, Review of solar cell temperature coefficients for space, <https://ntrs.nasa.gov/citations/19950014125>.
9. M. V. Khenkin, E. A. Katz, A. Abate, G. Bardizza, J. J. Berry, C. Brabec, F. Brunetti, V. Bulović, Q. Burlingame, A. Di Carlo, R. Cheacharoen, Y.-B. Cheng, A. Colmann, S. Cros, K. Domanski, M. Duszka, C. J. Fell, S. R. Forrest, Y. Galagan, D. Di Girolamo, M. Grätzel, A. Hagfeldt, E. von Hauff, H. Hoppe, J. Kettle, H. Köbler, M. S. Leite, S. Liu, Y.-L. Loo, J.



- M. Luther, C.-Q. Ma, M. Madsen, M. Manceau, M. Matheron, M. McGehee, R. Meitzner, M. K. Nazeeruddin, A. F. Nogueira, Ç. Odabaşı, A. Osherov, N.-G. Park, M. O. Reese, F. De Rossi, M. Saliba, U. S. Schubert, H. J. Snaith, S. D. Stranks, W. Tress, P. A. Troshin, V. Turkovic, S. Veenstra, I. Visoly-Fisher, A. Walsh, T. Watson, H. Xie, R. Yildirim, S. M. Zakeeruddin, K. Zhu and M. Lira-Cantu, *Nature Energy*, 2020, **5**, 35-49.
10. K. T. Tanko, Z. Tian, S. Raga, H. Xie, E. A. Katz and M. Lira-Cantu, *MRS Bulletin*, 2025, **50**, 512-525.
11. P. Holzhey and M. Saliba, *Journal of Materials Chemistry A*, 2018, **6**, 21794-21808.
12. Q. Jiang, R. Tirawat, R. A. Kerner, E. A. Gaulding, Y. Xian, X. Wang, J. M. Newkirk, Y. Yan, J. J. Berry and K. Zhu, *Nature*, 2023, **623**, 313-318.
13. R. K. Gupta, D. K. Kumar, V. Sudhakar, J. M. Beckedahl, A. Abate, E. A. Katz and I. Visoly-Fisher, *Advanced Energy Materials*, 2025, **15**, 2403844.
14. S. Su, T. Ahn and Y. Yang, *Advanced Functional Materials*, 2025, **35**, 2408480.
15. G. Y. Kim, A. Senocrate, T. Yang, G. Gregori, M. Grätzel and J. Maier, *Nat. Mater.*, 2018, **17**, 445.
16. Y.-C. Li, C. Ge, H.-Y. Song, P. Wang, X.-R. Ma and S.-B. Liu, *Journal of Applied Physics*, 2022, **132**, 013102.
17. L. E. Mundt and L. T. Schelhas, *Advanced Energy Materials*, 2020, **10**, 1903074.
18. A. Zohar, M. Kulbak, S. H. Turren-Cruz, P. K. Nayak, A. Kama, A. Hagfeldt, H. J. Snaith, G. Hodes and D. Cahen, *ACS applied materials & interfaces*, 2022, **14**, 34171-34179.
19. P. Lopez-Varo, M. Amara, S. Cacovich, A. Julien, A. Yaïche, M. Jouhari, J. Rousset, P. Schulz, J.-F. Guillemoles and J.-B. Puel, *Sustainable Energy & Fuels*, 2021, **5**, 5523-5534.
20. S. Tan, I. Yavuz, N. De Marco, T. Huang, S.-J. Lee, C. S. Choi, M. Wang, S. Nuryyeva, R. Wang, Y. Zhao, H.-C. Wang, T.-H. Han, B. Dunn, Y. Huang, J.-W. Lee and Y. Yang, *Advanced Materials*, 2020, **32**, 1906995.
21. Y. Wu, F. Xie, H. Chen, X. Yang, H. Su, M. Cai, Z. Zhou, T. Noda and L. Han, *Adv. Mater.*, 2017, **29**, 1701073.
22. H. B. Xie, Z. W. Wang, Z. H. Chen, C. Pereyra, M. Pols, K. Galkowski, M. Anaya, S. Fu, X. Y. Jia, P. Y. Tang, D. J. Kubicki, A. Agarwalla, H. S. Kim, D. Prochowicz, X. Borriese, M. Bonn, C. X. Bao, X. X. Sun, S. M. Zakeeruddin, L. Emsley, J. Arbiol, F. Gao, F. Fu, H. I. Wang, K. J. Tielrooij, S. D. Stranks, S. X. Tao, M. Grätzel, A. Hagfeldt and M. Lira-Cantu, *Joule*, 2021, **5**, 1246-1266.
23. C. Ma, F. T. Eickemeyer, S.-H. Lee, D.-H. Kang, S. J. Kwon, M. Grätzel and N.-G. Park, *Science*, 2023, **379**, 173-178.
24. C. Cheng, Y. Yao, L. Li, Q. Zhao, C. Zhang, X. Zhong, Q. Zhang, Y. Gao and K. Wang, *Nano Letters*, 2023, **23**, 8850-8859.
25. W.-H. Zhang, L. Chen, Z.-P. Zou, Z.-A. Nan, J.-L. Shi, Q.-P. Luo, Y. Hui, K.-X. Li, Y.-J. Wang, J.-Z. Zhou, J.-W. Yan and B.-W. Mao, *ACS applied materials & interfaces*, 2022, **14**, 31911-31919.
26. M. Karimipour, A. Paingott Parambil, K. Tabah Tanko, T. Zhang, F. Gao and M. Lira-Cantu, *Advanced Energy Materials*, 2023, **13**, 2301959.
27. A. Bou, A. Pockett, D. Raptis, T. Watson, M. J. Carnie and J. Bisquert, *J Phys Chem Lett*, 2020, **11**, 8654-8659.
28. F. Ebadi, M. Aryanpour, R. Mohammadpour and N. Taghavinia, *Scientific Reports*, 2019, **9**, 11962.
29. S. R. R. Kenedy T. Tanko, Naji Vahedigharehchopogh, Fanny Baumann, Masoud Karimipour, Ramsés Alejandro Miranda-Gamboa, Monica Lira-Cantú*, *Solar RRL*, 2025 (accepted), DOI: 10.1002/solr.202500162, <https://doi.org/10.1039/D5EL00104H>
30. L. Contreras-Bernal, S. Ramos-Terrón, A. Riquelme, P. P. Boix, J. Idigoras, I. Mora-Seró and J. A. Anta, *Journal of Materials Chemistry A*, 2019, **7**, 12191-12200.
31. O. Almora, P. López-Varo, R. Escalante, J. Mohanraj, L. F. Marsal, S. Olthof and J. A. Anta, *Journal of Applied Physics*, 2024, **136**.
32. O. Almora, K. T. Cho, S. Aghazada, I. Zimmermann, G. J. Matt, C. J. Brabec, M. K. Nazeeruddin and G. Garcia-Belmonte, *Nano Energy*, 2018, **48**, 63-72.
33. D. A. Jacobs, H. Shen, F. Pfeffer, J. Peng, T. P. White, F. J. Beck and K. R. Catchpole, *Journal of Applied Physics*, 2018, **124**.
34. M. T. Neukom, A. Schiller, S. Züfle, E. Knapp, J. Ávila, D. Pérez-del-Rey, C. Dreessen, K. P. S. Zanoni, M. Sessolo, H. J. Bolink and B. Ruhstaller, *ACS applied materials & interfaces*, 2019, **11**, 23320-23328.
35. S. Lammar, R. Escalante, A. J. Riquelme, S. Jenatsch, B. Ruhstaller, G. Oskam, T. Aernouts and J. A. Anta, *Journal of Materials Chemistry A*, 2022, **10**, 18782-18791.
36. D. Moia, I. Gelmetti, P. Calado, W. Fisher, M. Stringer, O. Game, Y. Hu, P. Docampo, D. Lidzey, E. Palomares, J. Nelson and P. R. F. Barnes, *Energy & Environmental Science*, 2019, **12**, 1296-1308.
37. C. Aranda, J. Bisquert and A. Guerrero, *The Journal of chemical physics*, 2019, **151**, 124201.
38. A. Guerrero, J. Bisquert and G. Garcia-Belmonte, *Chemical Reviews*, 2021, **121**, 14430-14484.
39. E. von Hauff and D. Klotz, *Journal of Materials Chemistry C*, 2022, **10**, 742-761.
40. A. Dualeh, T. Moehl, N. Tetreault, J. Teuscher, P. Gao, M. K. Nazeeruddin and M. Grätzel, *ACS nano*, 2014, **8**, 362-373.
41. J. Torres, I. Zarazua, D. Esparza, J. M. Rivas, M. Saliba, I. Mora-Seró, S.-H. Turren-Cruz and A. Abate, *ACS Applied Energy Materials*, 2022, **5**, 12545-12552.
42. S. D. Stranks, R. L. Z. Hoyer, D. W. Di, R. H. Friend and F. Deschler, *Advanced Materials*, 2019, **31**.
43. M. Ledinsky, T. Schönfeldová, J. Holovský, E. Aydin, Z. Hájková, L. Landová, N. Neyková, A. Fejfar and S. De Wolf, *The Journal of Physical Chemistry Letters*, 2019, **10**, 1368-1373.
44. J. Xu, S. Yu, X. Shang and X. Chen, *Advanced Photonics Research*, 2023, **4**, 2200193.
45. M. Wang, Z. Yang, Y. Chen, L. Shi, K. Cao, Y. Liang, G. Cao, X. Li and L. Qin, *Solar Energy Materials and Solar Cells*, 2025, **282**, 113393.
46. T. Kirchartz, J. A. Márquez, M. Stollerfoht and T. Unold, *Advanced Energy Materials*, 2020, **10**, 1904134.
47. M. Dailey, Y. Li and A. D. Printz, *ACS Omega*, 2021, **6**, 30214-30223.
48. C. Zhu, X. Niu, Y. Fu, N. Li, C. Hu, Y. Chen, X. He, G. Na, P. Liu, H. Zai, Y. Ge, Y. Lu, X. Ke, Y. Bai, S. Yang, P. Chen, Y. Li, M. Sui, L. Zhang, H. Zhou and Q. Chen, *Nature Communications*, 2019, **10**, 815.
49. S. Ma, J. Tang, G. Yuan, Y. Zhang, Y. Wang, Y. Wu, C. Zhu, Y. Wang, S. Wu, Y. Lu, S. Chi, T. Song, H. Zhou, M. Sui, Y. Li and Q. Chen, *ENERGY & ENVIRONMENTAL MATERIALS*, 2024, **7**, e12739.
50. G. G. Njema, J. K. Kibet and S. M. Ngari, *Measurement: Energy*, 2024, **2**, 100005.



51. S. N. Habisreutinger, N. K. Noel and H. J. Snaith, *ACS Energy Letters*, 2018, **3**, 2472-2476.
52. R. García-Rodríguez, A. J. Riquelme, M. Cowley, K. Valadez-Villalobos, G. Oskam, L. J. Bennett, M. J. Wolf, L. Contreras-Bernal, P. J. Cameron, A. B. Walker and J. A. Anta, *Energy Technology*, 2022, **10**, 2200507.
53. W. Clarke, M. V. Cowley, M. J. Wolf, P. Cameron, A. Walker and G. Richardson, *Journal of Applied Physics*, 2023, **133**.
54. F. Wu, R. Pathak, K. Chen, G. Wang, B. Bahrami, W.-H. Zhang and Q. Qiao, *ACS Energy Letters*, 2018, **3**, 2457-2460.
55. D. A. Shohonov, D. B. Migas, A. B. Filonov, V. E. Borisenko, R. Takabe and T. Suemasu, *Thin Solid Films*, 2019, **686**, 137436.
56. S. Kim, S. Bae, S. W. Lee, K. Cho, K. D. Lee, H. Kim, S. Park, G. Kwon, S. W. Ahn and H. M. Lee, *Sci. Rep.*, 2017, **7**, 1200.
57. S. Reichert, Q. An, Y. W. Woo, A. Walsh, Y. Vaynzof and C. Deibel, *Nat Commun*, 2020, **11**, 6098.
58. S. Kim, J. H. Jang, Z. Wu, M. J. Lee, H. Y. Woo and I. Hwang, *Small*, 2021, **17**.
59. C. Eames, J. M. Frost, P. R. F. Barnes, B. C. O'Regan, A. Walsh and M. S. Islam, *Nature Communications*, 2015, **6**, 7497.
60. M. H. Futscher, M. K. Gangishetty, D. N. Congreve and B. Ehrler, *The Journal of chemical physics*, 2020, **152**.
61. P. Srivastava, R. Kumar and M. Bag, *Physical chemistry chemical physics : PCCP*, 2021, **23**, 10936-10945.
62. A. D. Sheikh, R. Munir, M. A. Haque, A. Bera, W. Hu, P. Shaikh, A. Amassian and T. Wu, *ACS applied materials & interfaces*, 2017, **9**, 35018-35029.
63. A. M. Soufiani, Z. Hameiri, S. Meyer, S. Lim, M. J. Y. Tayebjee, J. S. Yun, A. Ho-Baillie, G. J. Conibeer, L. Spiccia and M. A. Green, *Advanced Energy Materials*, 2017, **7**.
64. A. D. Bui, N. Mozaffari, T. N. Truong, T. Duong, K. J. Weber, T. P. White, K. R. Catchpole, D. Macdonald and H. T. Nguyen, *Prog Photovoltaics*, 2022, **30**, 1038-1044.
65. A. A. B. Baloch, F. H. Alharbi, G. Grancini, M. I. Hossain, M. K. Nazeeruddin and N. Tabet, *J Phys Chem C*, 2018, **122**, 26805-26815.
66. M. Lira-Cantú, *Nature Energy*, 2017, **2**, 17115.
67. Z. Fan, H. Xiao, Y. Wang, Z. Zhao, Z. Lin, H.-C. Cheng, S.-J. Lee, G. Wang, Z. Feng, W. A. Goddard, Y. Huang and X. Duan, *Joule*, 2017, **1**, 548-562.
68. E. J. Juarez-Perez, L. K. Ono, M. Maeda, Y. Jiang, Z. Hawash and Y. Qi, *Journal of Materials Chemistry A*, 2018, **6**, 9604-9612.
69. A. Senocrate, G. Y. Kim, M. Grätzel and J. Maier, *ACS Energy Letters*, 2019, **4**, 2859-2870.
70. T. W. Kim, N. Shibayama, L. Cojocar, S. Uchida, T. Kondo and H. Segawa, *Advanced Functional Materials*, 2018, **28**, 1804039.
71. D. B. Khadka, Y. Shirai, M. Yanagida and K. Miyano, *ACS Applied Energy Materials*, 2021, **4**, 11121-11132.
72. I. S. Zhidkov, D. W. Boukhvalov, A. F. Akbulatov, L. A. Frolova, L. D. Finkelstein, A. I. Kukharensko, S. O. Cholakh, C.-C. Chueh, P. A. Troshin and E. Z. Kurmaev, *Nano Energy*, 2021, **79**, 105421.
73. S. R. Raga, L. K. Ono and Y. Qi, *Journal of Materials Chemistry A*, 2016, **4**, 2494-2500.
74. B. Yang, O. Dyck, W. Ming, M.-H. Du, S. Das, C. M. Rouleau, G. Duscher, D. B. Geohegan and K. Xiao, *ACS applied materials & interfaces*, 2016, **8**, 32333-32340.
75. T. Guo, P. Hu, L. Li, Z. Wang and L. Guo, *Chem*, 2023, **9**, 1080-1093.
 view Article Online
DOI: 10.1039/D5EL00104H
76. C. Bommier, D. Mitlin and X. Ji, *Progress in Materials Science*, 2018, **97**, 170-203.
77. D. A. Jacobs, Y. Wu, H. Shen, C. Barugkin, F. J. Beck, T. P. White, K. Weber and K. R. Catchpole, *Physical Chemistry Chemical Physics*, 2017, **19**, 3094-3103.
78. D. Meggiolaro, E. Mosconi and F. De Angelis, *ACS Energy Letters*, 2019, **4**, 779-785.



Data availability:

View Article Online
DOI: 10.1039/D5EL00104H

The data supporting this article have been included as part of the ESI. Data for this article, including the raw data for all figures in the article are available at CORA - Research Data Repository (RDR) at [<https://doi.org/10.34810/data2409>].

